

ARTICLE

Four-dimensional light shaping: manipulating ultrafast spatiotemporal foci in space and time

Bangshan Sun^{1,2}, Patrick S Salter¹, Clemens Roeder^{2,3}, Alexander Jesacher^{3,4}, Johannes Strauss^{2,4}, Johannes Heberle^{2,4}, Michael Schmidt^{2,4} and Martin J Booth^{1,4,5}

The spectral dispersion of ultrashort pulses allows the simultaneous focusing of light in both space and time, which creates so-called spatiotemporal foci. Such space–time coupling may be combined with the existing holographic techniques to give a further dimension of control when generating focal light fields. In the present study, it is shown that a phase-only hologram placed in the pupil plane of an objective and illuminated by a spatially chirped ultrashort pulse can be used to generate three-dimensional arrays of spatio-temporally focused spots. By exploiting the pulse front tilt generated at focus when applying simultaneous spatial and temporal focusing (SSTF), it is possible to overlap neighboring foci in time to create a smooth intensity distribution. The resulting light field displays a high level of axial confinement, with experimental demonstrations given through two-photon microscopy and the non-linear laser fabrication of glass.

Light: Science & Applications (2018) 7, 17117; doi:10.1038/lsa.2017.117; published online 12 January 2018

Keywords: laser material processing; light shaping; spatiotemporal focusing; ultrafast lasers

INTRODUCTION

The control of light in the focal region of a microscope objective lens is important in many different applications, ranging from imaging¹, to optical trapping² and laser fabrication³. Computer-generated holography has become a widespread tool to provide such control, particularly as it has developed in parallel with the increasing performance of liquid-crystal spatial light modulators, to the extent that the dynamic updating of complex light fields is now achievable in real time⁴. However, the development of control of such complex focal fields has mostly been confined to considerations of the three spatial dimensions.

When focusing an ultrashort pulse, an additional degree of freedom may be achieved. Dispersion of the spectral components of the light can stretch the pulse temporally, after which it may be compressed again to reconstitute the original short pulse. This process limits the interaction range of a non-linear process, such as two-photon fluorescence^{5–7}. Such temporal focusing may be combined with spatial focusing, for example, by using a grating followed by a positive lens, but in general, the two phenomena can be decoupled. Previously, such simultaneous spatiotemporal focusing (SSTF) was used to generate widefield focal intensity distributions with high uniformity and strong axial confinement, thus enabling rapid multiphoton imaging^{8–11} with the potential for use even deep inside scattering tissue^{12,13}. The spectral spread prior to focus also alleviates problems related to

non-linear propagation, such as filamentation, which can prove disastrous for laser processing through thick dielectrics^{14,15}. In addition, SSTF offers several additional levels of control over the ultrafast laser focus, including a controllable aspect ratio^{16,17} and an adjustable pulse front tilt (PFT)^{18–20}, leading to applications such as processing glass for microfluidics^{14,16} and biomedical tissue ablation²¹.

Parallelization is already a common concept for using conventional focusing to increase the processing speed in applications such as multiphoton microscopy²² and laser fabrication^{23–25}. SSTF has further advantages when generating such complex focal distributions. By shaping the light through holography^{12,26}, projection^{27–29} or generalized phase contrast³⁰ prior to the dispersive element, a patterned SSTF focus may be generated. Such continuous intensity distributions typically display poor axial resolution, but including SSTF in the optical system restores axial confinement at the focus. In this paper, we demonstrate that it is also possible to holographically shape the light after spectral dispersion of the pulse. We are able to create two- and three-dimensional arrays of SSTF spots using a phase-only hologram placed in the spatially chirped beam. In fact, using a hologram in this configuration gives an additional level of control of the light field. The inherent pulse front tilt associated with SSTF spots can be exploited to overlap neighboring foci such that multiple spots from a single pulse may overlap in space but be separate in time. Thus, the conventional limitations on holographic spot spacing due to

¹Department of Engineering Science, University of Oxford, Parks Road, Oxford OX1 3PJ, UK; ²Institute of Photonic Technologies, Friedrich-Alexander-University Erlangen-Nuremberg, Konrad-Zuse-Strasse 3/5, Erlangen 91052, Germany; ³Division of Biomedical Physics, Innsbruck Medical University, Mullerstrasse 44, Innsbruck 6020, Austria; ⁴Graduate School in Advanced Optical Technologies (SAOT), Friedrich-Alexander University Erlangen-Nuremberg, Paul-Gordan-Strasse 6, Erlangen 91052, Germany and ⁵Centre for Neural Circuits and Behaviour, University of Oxford, Mansfield Road, Oxford OX1 3SR, UK

Correspondence: MJ Booth, Email: martin.booth@eng.ox.ac.uk

Received 14 May 2017; revised 8 August 2017; accepted 8 August 2017; accepted article preview online 16 August 2017

The accepted article preview was available with the details: *Light: Science & Applications* (2018) 7, e17117; doi: 10.1038/lsa.2017.117

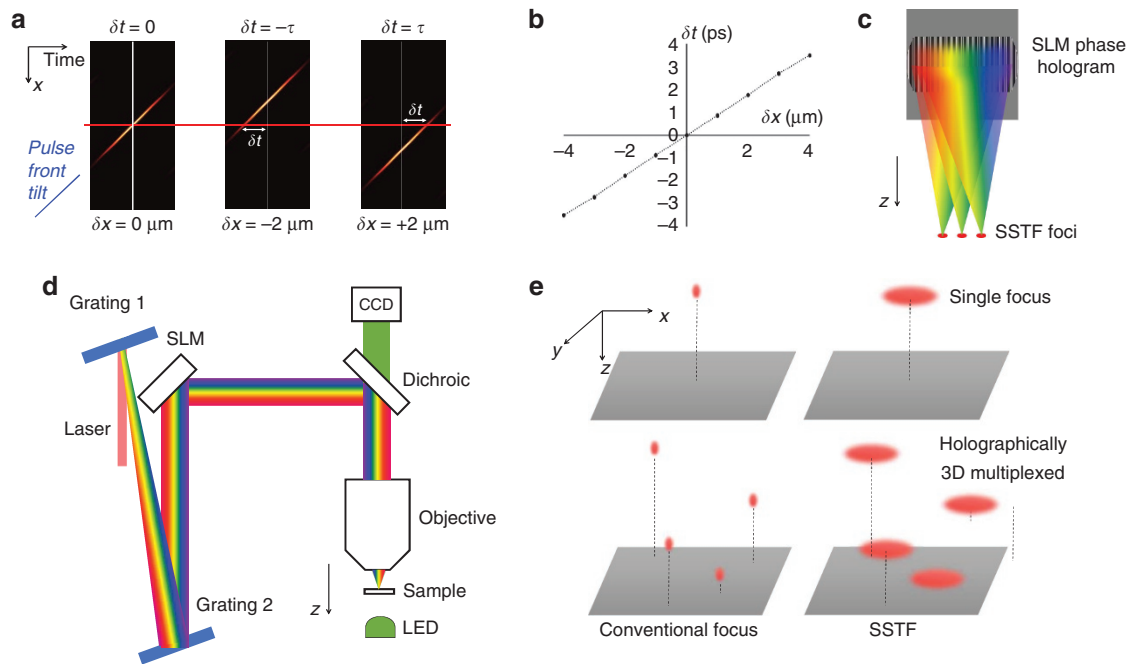


Figure 1 (a) Effect of a linear phase gradient on the SSTF focus. Images show simulated results of space–time (x, t) intensity variations of temporal foci. Left to right: no phase gradient, linear phase causing negative shift, linear phase causing positive shift. (b) Plot of lateral spatial shift versus on-axis temporal delay for an SSTF focus, with a varying magnitude of linear spectral phase applied. (c) Sketch illustrating the principle for creating a three-dimensional multiple SSTF array. The z -direction is the optical axis (light penetrating into the sample). (d) Experimental system for four-dimensional light shaping (a full diagram is provided in Supplementary Information Figure S1). (e) Sketch representing the relationship between ‘conventional focus’ and ‘SSTF’, as well as ‘single focus’ and ‘holographic 3D multiplexed’. SLM, Spatial Light Modulator.

mutual interference can be overcome through the simultaneous control of the intensity distribution in four dimensions: three of space and one of time.

MATERIALS AND METHODS

Holography in a spatially chirped beam

How can holographic elements be used to adjust the focus in the time dimension? It is already known that applying group velocity dispersion (GVD) to an ultrafast beam axially scans an SSTF focus³¹. This can be simply understood if the GVD corresponds to a quadratic spectral phase (that is, the phase shift ψ at a frequency ω is given by $\psi(\omega) \propto \omega^2$). In the pupil plane of the objective in an SSTF system, there is a uniform spatial chirp (such that $r(\omega) \propto \omega$, where r is the radial position in the pupil of a spectral component). Hence, $\psi(r) \propto r^2$, which shows that the GVD is equivalent to applying a quadratic phase in the objective pupil, which in the paraxial regime shifts the focus along the optical axis^{26,32,33}. Recent work has also shown that applying various phase-based aberrations in the pupil plane of an objective leads to some familiar focal distortion with reference to conventional focusing systems^{34–36}. What is the link between these spatial manipulations and temporal control?

It is instructive here to look at the application of a linear phase gradient to a spatially chirped beam in the pupil of an objective lens (in other words, $\psi(r) \propto r$). Figure 1a shows the space–time (x, t) intensity variation of an example SSTF focus. There is a strong pulse front tilt (PFT), which is characteristic of SSTF³⁷. As should be expected, the linear phase gradient causes a transverse shift of the focus. However, this phase gradient is also equivalent to a spectral phase $\psi(\omega) \propto \omega$. Therefore, from the Fourier shift theorem, one should also expect a temporal delay in the focus. This dual manifestation is apparent in the plot of Figure 1b, where we see that

the combination of the lateral shift and the PFT leads to a temporal delay on axis. Thus, we can see that it is indeed possible to translate a single SSTF focus in both space and time, with an appropriate phase applied to the pupil plane of the lens.

Since it is possible to translate an SSTF focus in three dimensions using a phase pattern placed in the spatially chirped beam, it is an obvious extension that a combination of gratings to direct foci to different locations within the focal region should enable the generation of multiple SSTF spots. The principle is illustrated in the sketch included in Figure 1c. The pattern displayed on the Spatial Light Modulator (SLM) modulates the phases of all spectral components, and each spectral component is diffracted by the unique local region of the hologram and propagates along several different beam paths into the focal region. The net effect of this is that there are several parts of the focal region where all spectral components overlap with the correct phase to form spatiotemporal foci. As a result, each spatiotemporal focal spot is expected to contain contributions from all spectral components across the whole pupil, thus confirming the simultaneous spatial and temporal focusing property for all of the spots. Furthermore, it should be possible within certain practical bounds to introduce desired spatial and temporal shifts to the different foci. The sketch in Figure 1e illustrates the relationship between the conventional focusing and the SSTF. A single focus and holographic 3D multiplexed foci are compared. Note that the foci sketched here would have circular cross-sections if viewed along the optical axis.

Experimental system

The experimental system is shown in Figure 1d. The ultrafast laser was a OneFive Origami XP, with the wavelength of 1030 nm, pulse duration of 350 fs, spectral bandwidth of <4 nm and tuneable repetition rate from 50 kHz to 1 MHz. The beam was spectrally

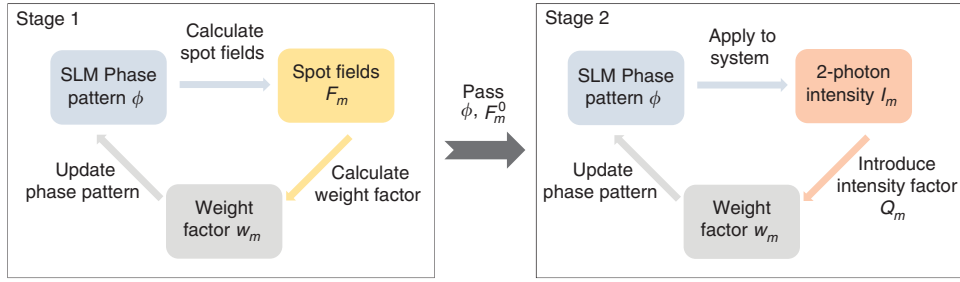


Figure 2 Flow chart illustrating the two-stage process for updating the phase pattern in the hologram design.

spread using two blazed gratings (Thorlabs GR25-0610, 600 grooves per mm, blazed for 1 μm wavelength light). The incident angle for both gratings was aligned to approach the Littrow Configuration ($17^\circ 27'$), giving a first-order diffraction efficiency of 85% per grating. The spectrally dispersed beam was then directed onto a phase-only liquid-crystal SLM (Hamamatsu X11840). The full width at half maximum (FWHM) of the beam in the unchirped direction D_x at the SLM was only ~ 3.1 mm, thus limiting the active area. This dimension D_x determines the monochromatic beam size at the pupil, which can be adjusted to control the lateral ellipticity of each SSTF focus^{16,17}. A smaller D_x extends the dimensions of the spatiotemporal focus axially and laterally (in a direction orthogonal to the spatial chirp)³⁴. A $4f$ system was used to image the SLM into the pupil of the objective lens (Zeiss EC Epiplan 50 \times , 0.75 NA and a pupil diameter of 4.95 mm). A 3D translation stage (Thorlabs 6-Axis NanoMax, MAX607/M) was used to control the motion of the sample. An LED-illuminated widefield optical microscope was integrated to image the focal region. A CCD camera (Lumenera Lm075M) was used for the detection of two-photon emission.

Hologram design

The phase patterns displayed on the SLM were designed by a Modified Weighted Gerchberg-Saxton method (MWGS)^{38,39}. Two stages of the algorithm were implemented to obtain the final phase pattern, as shown in Figure 2. Stage 1 updates the phase pattern based on the theoretical calculation of the intensity in the focal field. The phase pattern in iteration $p+1$ is updated by

$$\Phi^{p+1} = \arg \left[\sum_{m=1}^n \left\{ \exp[i\Delta_m] \times \frac{F_m^p}{|F_m^p|} \times w_m^p \right\} \right] \quad (1)$$

where weight factor w_m is defined as

$$w_m^p = w_m^{p-1} \times \frac{(\sum_{i=1}^n \{|F_m^p|\})/n}{|F_m^p|} \quad (2)$$

In the above equations, $\Delta_m(x, y)$ is the propagator function relating the spatial positions of each spot m in the focal field to pixels of the hologram in the back focal plane of the lens, compensating for any depth-dependent spherical aberration³⁹. F_m^p is the calculated amplitude of the field for spot m based on the phase in current iteration p , and n is the total number of spatiotemporal focal spots.

In Stage 1, the focal amplitude calculations were based on Fourier optics theory using practical parameters from the experimental system. The simulations of multiple widefield SSTF spots considered both phase modulation and spatial spectral chirp to increase the accuracy of the hologram calculation³⁴.

Stage 1 designs the initial hologram through pure theoretical simulation. In practice, imperfections of the optical system make it difficult to obtain a high-quality SSTF, as predicted by theory. We

therefore introduced an additional stage to optimize the hologram. Stage 2 of the algorithm updates the phase pattern based on the experimental measurement of two-photon fluorescence from each focus^{40,41}. We also introduced an intensity factor, Q_m , which allows a different target intensity for each spot. Such an intensity factor could just have been easily included in Stage 1 of the calculation⁴², but by including it in Stage 2, it can remove any relation to the non-linearity of the light-matter interaction. The measured two-photon fluorescence intensity of each spatiotemporal focus in iteration q is represented as I_m^q for spot m . The phase pattern in iteration $q+1$ is then updated by

$$\Phi^{q+1} = \arg \left[\sum_{m=1}^n \left\{ \exp[i\Delta_m] \times \frac{F_m^0}{|F_m^0|} \times w_m^q \right\} \right] \quad (3)$$

where F_m^0 is the last spot field calculated in Stage 1. The weight factor w_m^q is defined as

$$w_m^q = w_m^{q-1} \times \frac{(\sum_{i=1}^n \{I_m^q/Q_m\})/n}{I_m^q/Q_m} \quad (4)$$

As shown in the above equations, in contrast to Stage 1, the phase of each spot (which is determined by $\exp[i\Delta_m] \times \frac{F_m^0}{|F_m^0|}$) is fixed in each iteration of Stage 2. Only the weight factor w_m^q is updated in Stage 2 until all spots reach the target values for the two-photon fluorescence intensity. In our experiments, 1–5 iterations of Stage 2 were usually required to obtain good uniformity, with the number of iterations being dependent on the system configuration. As the purpose of Stage 2 is to resolve any problem resulting from system imperfections, this stage only needs to be implemented once. The generated phase correction could subsequently be used for most samples.

The calculation process of each stage is not particularly computationally intensive and typically takes less than one minute. The duration is nearly independent of whether the array is 2D or 3D. By implementing the algorithm on the GPU, the calculation speed could be significantly enhanced to, in theory, allow the dynamic modulation of the individual spots⁴. The time-limiting factor in updating the spot pattern would then become the refresh rate of the SLM. Using our technique here, a nematic liquid-crystal SLM is needed to achieve grayscale phase control. Nematic liquid-crystal SLMs typically have a refresh rate of 60 Hz, but it has recently been shown that by using over-drive techniques, response times of ~ 1 ms can be achieved⁴³, moving into a regime where high-speed dynamic updates of the spot pattern are possible.

Measurement of focal intensity distribution

Two methods were employed to measure the focal intensity distribution of the generated spots. In the first, a mirror was aligned at the focal plane of the objective lens and images were taken using the

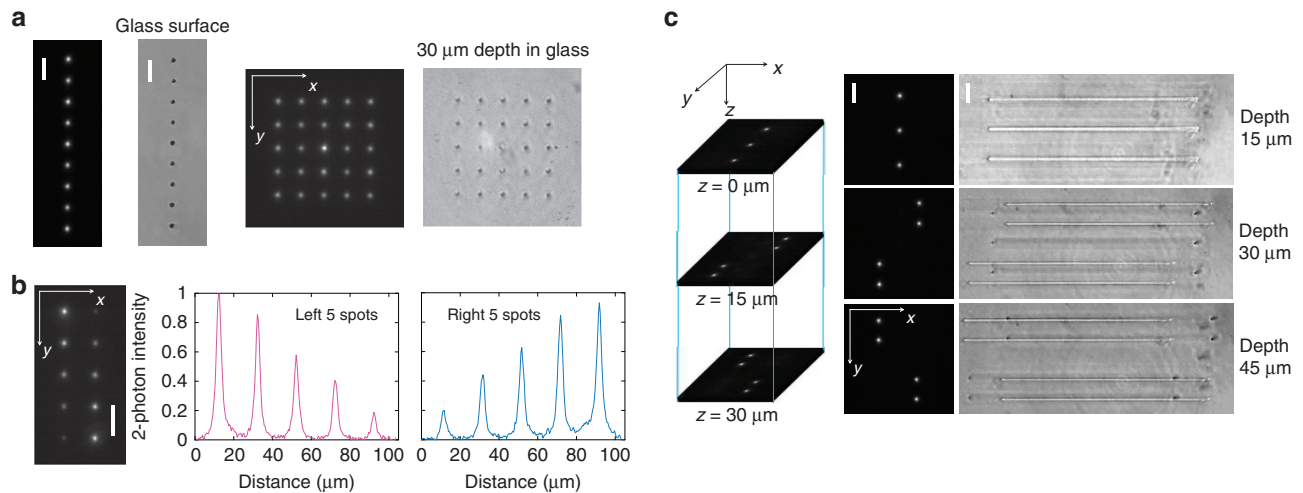


Figure 3 (a) The images of two-photon emission and fabrication in glass for a 2D 1×9 array and a 2D 5×5 SSTF multiple focal array. The images from left to right: two-photon image of 1×9 array, single-exposure fabrication on the glass surface of 1×9 array, two-photon image of 5×5 array, single exposure fabrication in glass with $30 \mu\text{m}$ depth of 5×5 array. Scale bar is $15 \mu\text{m}$. (b) Left: Image of two-photon fluorescence arising from an SSTF array with designed intensity variation between each spot. Scale bar is $20 \mu\text{m}$. Right: The line plots show an intensity profile along the central line of the left- and right-hand sets of 5 foci. The constant background offset was subtracted in the plots. (c) 3D multiple focal array of 11 spatiotemporal spots that were distributed at three different axial planes. The images of two-photon emission and fabrication in glass are presented. Scale bar is $15 \mu\text{m}$. The SLM phases used to create these temporal arrays are presented in Supplementary Information Figure S3.

integrated widefield optical microscope. These images were linear in the focal intensity and hence did not reveal the temporal focusing aspect of the arrangement. Therefore, we additionally probed the non-linear response to the SSTF foci by monitoring the fluorescence emission due to two-photon excitation of a uniform fluorescent volume. The sample consisted of an aqueous solution of propidium iodide (PI, Sigma Aldrich P4170) with a concentration of 10 mg/ml , sealed between a microscope slide and a cover slip. The emitted fluorescence was captured on the CCD, with an additional short-pass filter inserted to block any back-scattered light from the laser. Due to the well-confined excitation and high concentration of the PI solution, the two-photon fluorescence emission was sufficiently strong to be detected in standard video mode of the CCD camera. The two-photon nature of the excitation was confirmed by the quadratic dependence of the fluorescence intensity on the illumination power. The axial extent of the foci was estimated by measuring the edge response obtained by scanning the sample along the optical axis, so that the foci traversed the interface between the cover slip and the PI solution (Supplementary Information Figure S2).

For all of the following results, the system was configured such that each of the SSTF foci had a lateral full width at half maximum (FWHM) diameter of $2.5 \mu\text{m}$, which was measured consistently across all experiments. From the two-photon edge response, the axial FWHM in water was estimated to be $\sim 7.5 \mu\text{m}$. These values can be compared with calculations for an objective lens with an NA of 0.2 by using conventional focusing: the lateral FWHM would again be $2.5 \mu\text{m}$, whereas the axial FWHM would be approximately eight times larger, at $60 \mu\text{m}$. The confinement of the non-linear effect along the axial direction clearly shows the non-conventional and spatiotemporal nature of the focus.

Due to the limitation on pulse energy from the laser source, we opted for relatively small temporal foci in these demonstrations to maximize the capacity for parallelization. However, we note that by adjusting the beam size directly after the laser source, it is possible to vary the spatial extent of the illumination at the pupil and hence change the lateral size of the temporal foci. In such a manner, our

experiments showed that the lateral size of the foci could be increased to $10 \mu\text{m}$ FWHM while still successfully generating an array of temporal foci.

Direct laser writing

A further application that highlights the temporal compression of the pulse in SSTF is direct laser writing inside transparent materials, which relies on non-linear absorption at the focus⁴⁴. Fabrication was conducted either on the surface or inside standard microscope glass slides (CarlRoth 0656.1). A scan speed of $20 \mu\text{m/s}$ was used to draw continuous lines within the glass with a laser repetition rate of 50 kHz . The pulse energy was adjusted as necessary for each experiment.

RESULTS AND DISCUSSION

Holographically generated SSTF focal arrays

Figure 3 shows various demonstrations of holographically multiplexed spatiotemporal foci in two and three dimensions. Figure 3a shows images of the two-photon fluorescence and direct laser writing in glass with 1×9 and 5×5 arrays of SSTF foci. The 1×9 SSTF array was designed for fabrication on the glass surface, without the correction of refractive index mismatch, whereas the 5×5 temporal focal array was designed for fabrication at a $30 \mu\text{m}$ depth inside the glass with an incorporated correction of index-mismatch aberration. The intensity factor Q_m (equation (4)) was set to be one to achieve high uniformity for all of the SSTF foci. As a result, in both arrays, all of the SSTF spots exhibited similar two-photon intensity and similar properties in fabrication. It is notable that the zero order, comprising light that is not modulated by the SLM phase pattern, becomes stronger when the focal array stretches along both the x and y directions. To suppress the intensity of the zero order, the hologram may be designed to generate an additional spot that overlaps the zero order and leads to destructive interference³⁹. It is thus possible to reduce the zero order in the 5×5 array such that the intensity of the central spot is not significantly different than the intensities of the other spots (Supplementary Information Figure S4).

We demonstrate that the intensity of each SSTF spot can also be individually controlled. This relies on the introduction of the intensity factor in Stage 2 of the phase pattern design. We designed a 2×5 temporal focal array to demonstrate this ability, as shown in Figure 3b. The intensity factor Q_m (equation (4)) was set to [5, 4, 3, 2, 1] and [1, 2, 3, 4, 5] for the spot vectors on the left and right sides, respectively. After a few iterations in Stage 2, the two-photon intensity of each spot in the 2×5 array reached the desired relative value. We note that the spot intensities do not necessarily have to be linearly related. Any combination of relative intensities can be achieved by adjusting the intensity factor Q_m .

A three-dimensional spatiotemporal focal array was designed and presented in Figure 3c. Similarly, the intensity factors Q_m (equation (4)) were set to one to achieve high uniformity in two-photon intensity. The 11 temporal foci were designed to distribute in three different lateral planes, spaced axially by a distance of $15 \mu\text{m}$. In the nominal focal plane, three temporal spots are located along the y direction. In the planes that were $15 \mu\text{m}$ and $30 \mu\text{m}$ below the nominal focal plane, four SSTF spots were distributed in both the x and y directions, as shown in Figure 3(c). The two-photon fluorescence images in the $z=15 \mu\text{m}$ and $z=30 \mu\text{m}$ planes were captured by refocusing the integrated inspection microscope independent of the temporal focus system. The refractive index-mismatch aberrations were all corrected in the hologram design for 11 SSTF spots, and the array was designed for fabrication in glass at a mean depth of $30 \mu\text{m}$. As shown in the right images of Figure 3(c), with one single pass of the glass sample, 11 lines with different starting points were fabricated at three different depths at the same time.

In the design of a 3D SSTF focal array, it is notable that if several spots have the same x and y positions, the spots had to have considerable separation along the z -direction (at least 5–10 times the FWHM axial resolution) to achieve distinct temporal foci with high uniformity of intensity. The required separation is related to the monochromatic beam size in the objective pupil (that is, the NA for each spectral component) and, hence, the transverse size of the foci. We note that this distance is greater than that needed in holographic arrays using conventional focusing due to the reduced effective NA of each spectral component in SSTF.

Interleaving foci in space and time

We have shown that it is possible to generate multiple SSTF spots in 3D by using a hologram in the spatially chirped beam. We now explore how the additional consideration of the time dimension leads to extra flexibility in the implementation of parallelized SSTF.

We first consider a linear array of nine SSTF spots arranged along the direction perpendicular to the spatial chirp (i.e., parallel to the x axis) with a separation of $4 \mu\text{m}$. The experimentally measured spatial intensity distributions are shown in Figure 4a along with the theoretically calculated space–time distribution. As expected, there is mutual interference between the spots, and the definition of the spot array is lost because the light arrives simultaneously at each point across the array. However, if we create another array, with the same spacing but oriented along the spatial chirp direction (y axis), there is minimal interference, and the array of nine spots is still clearly defined (Figure 4b). The reason for this lack of interference can be explained by the strong pulse front tilt (PFT) present in SSTF foci^{18–20}. The space–time plot shows clearly that due to the PFT, there is no overlap between the foci when considered in 4D. Instead, the foci are interleaved in space time, and there is no interference between the spots.

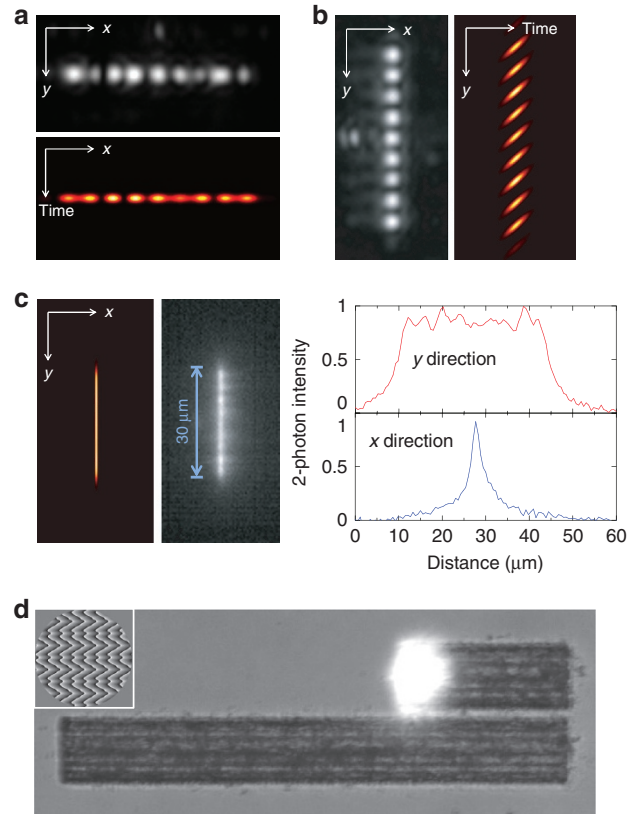


Figure 4 (a) Top: Image of nine spatiotemporal spots in an array orthogonal to the direction of spatial chirp (x axis). Bottom: simulation of intensity profile in the time domain (x -time profile). The distance between each spot is $4 \mu\text{m}$. (b) Left: Image of nine spatiotemporal spots in an array along the direction of spatial chirp (y axis). Right: simulation of intensity profile in the time domain (y -time profile). The distance between each spot is $4 \mu\text{m}$. (c) Left: simulation of time-averaged two-photon intensity for line temporal focusing with nine spots, assuming the spots are separated by a distance of $3 \mu\text{m}$. Middle: experimental two-photon image taken in the fluorescent dye sample. Right: plots of the two-photon intensities along the x and y axes. The RMS error of two-photon emission for the $30 \mu\text{m}$ uniform area along the y axis is 0.046 in normalized intensity. (d) The application of the uniform intensity temporal line to direct laser writing on the surface of glass. The focal plasma is the white region. Inset: phase pattern used to create this uniform intensity temporal line.

This space–time interleaving means that it is possible to generate an extended line of approximately uniform time-averaged intensity using multiple SSTF spots positioned along the direction of the spatial chirp. This can be realized either by reducing the distance between each spot or increasing the focal spot size by reducing the input monochromatic beam size. In this way, adjacent spots can be spatially overlapped with minimal interference between them, as demonstrated by the simulation results in Figure 4c. In practice, we chose an appropriate spacing distance of $3 \mu\text{m}$, and the focal spots were made broader by the inclusion of an adjustable iris before the gratings. On the one hand, a small distance would introduce a larger number of focal spots, thus increasing the difficulty in making sure all spots have the same intensity within a complex SLM phase. On the other hand, a more extended focal size does not necessarily bring better performance of a uniform line (Supplementary Information Figure S6). Figure 4c presents the two-photon fluorescence generated using the focal strip, which extends along the spatial chirp direction (y axis) for more than $30 \mu\text{m}$. This remarkable result, where it is possible to spatially overlap several foci

from the same pulse, is only possible due to spatiotemporal interleaving at the focus. It is not possible to generate such a uniform line focus in the orthogonal direction, in which there is no PFT.

One application of this uniform intensity line focus is in wide-area laser machining, where ‘flat top’ beams are commonly sought. As shown in Figure 4(d), a region with size $30 \times 200 \mu\text{m}$ was fabricated with a single pass of the sample. We note that laser processing with a conventional line focus that is generated by, for example, a cylindrical lens tends to produce stronger material modification in the central area, where the laser intensity is higher. In contrast, the spatiotemporal interleaving method generates an intensity distribution with a flatter top, leading to a fabricated region that is uniform across the whole area, thereby maximizing the processing efficiency. SSTF itself should theoretically not require any more laser power than conventional focusing, although in practice, slightly more power is indeed needed due to system imperfections. The added system complexity can be offset by the additional benefits incurred by SSTF across the laser processing and microscopy applications, and there should not be a difference in laser material processing speed between the methods.

CONCLUSION

We have demonstrated that multiple SSTF foci may be generated in 2D and 3D through an appropriately designed diffractive holographic element illuminated by a spatially chirped beam. The spatiotemporal nature of these foci has been confirmed through two-photon imaging and direct laser writing. Thus, it should be possible to combine the known advantageous aspects of SSTF (e.g., reduced scattering effect, non-linear effects, controllable aspect ratio, adjustable pulse front tilt) with the ability to increase the process speed through parallelization. In addition, we discovered a unique characteristic of multiplexed SSTF foci: the spatiotemporal coupling may be exploited to interleave foci in space time. This permits spatial overlap of adjacent foci with minimal interference. It is thus possible to generate a uniform ‘flat top’ intensity extended line focus based upon the inherent pulse front tilt present in SSTF. This ability offers an additional degree of freedom over conventional holographic spot arrays with conventional focusing, where there is a limitation on how closely spaced the spots may be⁴⁵. If they are positioned closer than ~ 3 Airy units of each other, mutual interference causes significant distortion of the desired intensity profile, in effect resulting in non-uniformity of the illuminated area. Appropriate placement of the foci in 4D allows us to avoid this problem, thus opening applications in non-linear imaging and laser processing.

CONFLICT OF INTEREST

The authors declare no conflict of interest.

ACKNOWLEDGEMENTS

The authors gratefully acknowledge experimental guidance and useful discussion from Marcus Baum and Tom Hafner. The research was supported through funding from the Erlangen Graduate School in Advanced Optical Technologies (SAOT) by the German Research Foundation (DFG) in the framework of the German excellence initiative, the Leverhulme Trust (RPG-2013-044) and by the European Research Council (ERC) under the Horizon 2020 research and innovation programme (grant agreement no. 695140).

- 3 Sugioka K, Cheng Y. Femtosecond laser three-dimensional micro- and nanofabrication. *Appl Phys Rev* 2014; **1**: 041303.
- 4 Preece D, Bowman R, Linnenberger A, Gibson G, Serati D *et al*. Increasing trap stiffness with position clamping in holographic optical tweezers. *Opt Express* 2009; **17**: 22718–22725.
- 5 Zhu GH, van Howe J, Durst M, Zipfel W, Xu C. Simultaneous spatial and temporal focusing of femtosecond pulses. *Opt Express* 2005; **13**: 2153–2159.
- 6 Oron D, Silberberg Y. Spatiotemporal coherent control using shaped, temporally focused pulses. *Opt Express* 2005; **13**: 9903–9908.
- 7 Durfee CG, Squier JA. Breakthroughs in photonics 2014: spatiotemporal focusing: advances and applications. *IEEE Photonics J* 2014; **7**: 0700806.
- 8 Choi H, Yew EYS, Hallacoglu B, Fantini S, Sheppard CJR *et al*. Improvement of axial resolution and contrast in temporally focused widefield two-photon microscopy with structured light illumination. *Biomed Opt Exp* 2013; **4**: 995–1005.
- 9 Lien CH, Lin CY, Chen SJ, Chien FC. Dynamic particle tracking via temporal focusing multiphoton microscopy with astigmatism imaging. *Opt Express* 2014; **22**: 27290–27299.
- 10 Dana H, Marom A, Paluch S, Dvorkin R, Brosh I *et al*. Hybrid multiphoton volumetric functional imaging of large-scale bioengineered neuronal networks. *Nat Commun* 2014; **5**: 3997.
- 11 Song QY, Nakamura A, Hirosawa K, Isobe K, Midorikawa K *et al*. Two-dimensional spatiotemporal focusing of femtosecond pulses and its applications in microscopy. *Rev Sci Instrum* 2015; **86**: 083701.
- 12 Papagiakoumou E, Bègue A, Leshem B, Schwartz O, Stell BM *et al*. Functional patterned multiphoton excitation deep inside scattering tissue. *Nat Photonics* 2013; **7**: 274–278.
- 13 Dana H, Kruger N, Ellman A, Shoham S. Line temporal focusing characteristics in transparent and scattering media. *Opt Express* 2013; **21**: 5677–5687.
- 14 Vitek DN, Adams DE, Johnson A, Tsai PS, Backus S *et al*. Temporally focused femtosecond laser pulses for low numerical aperture micromachining through optically transparent materials. *Opt Express* 2010; **18**: 18086–18094.
- 15 Kammel R, Ackermann R, Thomas J, Götze J, Skupin S *et al*. Enhancing precision in fs-laser material processing by simultaneous spatial and temporal focusing. *Light Sci Appl* 2014; **3**: e169.
- 16 He F, Xu H, Cheng Y, Ni JL, Xiong H *et al*. Fabrication of microfluidic channels with a circular cross section using spatiotemporally focused femtosecond laser pulses. *Opt Lett* 2010; **35**: 1106–1108.
- 17 He F, Cheng Y, Lin JT, Ni JL, Xu ZZ *et al*. Independent control of aspect ratios in the axial and lateral cross sections of a focal spot for three-dimensional femtosecond laser micromachining. *N J Phys* 2011; **13**: 083014.
- 18 Vitek DN, Block E, Bellouard Y, Adams DE, Backus S *et al*. Spatio-temporally focused femtosecond laser pulses for nonreciprocal writing in optically transparent materials. *Opt Express* 2010; **18**: 24673–24678.
- 19 Block E, Thomas J, Durfee C, Squier J. Integrated single grating compressor for variable pulse front tilt in simultaneously spatially and temporally focused systems. *Opt Lett* 2014; **39**: 6915–6918.
- 20 Zhang S, Wyrowski F, Kammel R, Nolte S. A brief analysis on pulse front tilt in simultaneous spatial and temporal focusing. Proceedings of SPIE 8972, Frontiers in Ultrafast Optics: Biomedical, Scientific, and Industrial Applications XIV, 89721B, 7 March 2014; San Francisco, CA, USA. SPIE: San Francisco, CA, USA, 2014.
- 21 Block E, Greco M, Vitek D, Masihzadeh O, Ammar DA *et al*. Simultaneous spatial and temporal focusing for tissue ablation. *Biomed Opt Exp* 2013; **4**: 831–841.
- 22 Poland SP, Krstajić N, Coelho S, Tyndall D, Walker RJ *et al*. Time-resolved multifocal multiphoton microscope for high speed FRET imaging in vivo. *Opt Lett* 2014; **39**: 6013–6016.
- 23 Waller EH, von Freymann G. Multi foci with diffraction limited resolution. *Opt Express* 2013; **21**: 21708–21713.
- 24 Lin H, Gu M. Creation of diffraction-limited non-Airy multifocal arrays using a spatially shifted vortex beam. *Appl Phys Lett* 2013; **102**: 084103.
- 25 Hasegawa S, Ito H, Toyoda H, Hayasaki Y. Massively parallel femtosecond laser processing. *Opt Express* 2016; **24**: 18513–18524.
- 26 Hernandez O, Papagiakoumou E, Tanese D, Felin K, Wyart C *et al*. Three-dimensional spatiotemporal focusing of holographic patterns. *Nat Commun* 2016; **7**: 11928.
- 27 Papagiakoumou E, de Sars V, Oron D, Emiliani V. Patterned two-photon illumination by spatiotemporal shaping of ultrashort pulses. *Opt Express* 2008; **16**: 22039–22047.
- 28 Kim D, So TC. High-throughput three-dimensional lithographic microfabrication. *Opt Lett* 2010; **35**: 1602–1604.
- 29 Li YC, Cheng LC, Chang CY, Lien CH, Campagnola PJ *et al*. Fast multiphoton microfabrication of freeform polymer microstructures by spatiotemporal focusing and patterned excitation. *Opt Express* 2012; **20**: 19030–19038.
- 30 Papagiakoumou E, Anselmi F, Bègue A, de Sars V, Glückstad J *et al*. Scanless two-photon excitation of channelrhodopsin-2. *Nat Methods* 2010; **7**: 848–854.
- 31 Durst ME, Zhu GH, Xu C. Simultaneous spatial and temporal focusing for axial scanning. *Opt Express* 2006; **14**: 12243–12254.
- 32 Leshem B, Hernandez O, Papagiakoumou E, Emiliani V, Oron D. When can temporally focused excitation be axially shifted by dispersion? *Opt Express* 2014; **22**: 7087–7098.
- 33 Žurauskas M, Barnstedt O, Frade-Rodríguez M, Waddell S, Booth MJ. Rapid adaptive remote focusing microscope for sensing of volumetric neural activity. *Biomed Opt Exp* 2017; **8**: 4369–4379.
- 34 Sun BS, Salter PS, Booth MJ. Effects of aberrations in spatiotemporal focusing of ultrashort laser pulses. *J Opt Soc Am A* 2014; **31**: 765–772.

1 Maurer C, Jesacher A, Bernet S, Ritsch-Marte M. What spatial light modulators can do for optical microscopy. *Laser Photonics Rev* 2011; **5**: 81–101.

2 Curtis JE, Koss BA, Grier DG. Dynamic holographic optical tweezers. *Opt Commun* 2002; **207**: 169–175.

- 35 Chang CY, LCheng LC, Su HW, Hu YY, Cho KC *et al*. Wavefront sensorless adaptive optics temporal focusing-based multiphoton microscopy. *Biomed Opt Express* 2014; **5**: 1768–1777.
- 36 Greco MJ, Block E, Meier AK, Beaman A, Cooper S *et al*. Spatial-spectral characterization of focused spatially chirped broadband laser beams. *Appl Opt* 2015; **54**: 9818–9822.
- 37 Durfee CG, Greco MJ, Block E, Vitek D, Squier JA. Intuitive analysis of space-time focusing with double-ABCD calculation. *Opt Express* 2012; **20**: 14244–14259.
- 38 Di Leonardo R, Ianni F, Ruocco G. Computer generation of optimal holograms for optical trap arrays. *Opt Express* 2007; **15**: 1913–1922.
- 39 Jesacher A, Booth MJ. Parallel direct laser writing in three dimensions with spatially dependent aberration correction. *Opt Express* 2010; **18**: 21090–21099.
- 40 Hasegawa S, Hayasaki Y. Second-harmonic optimization of computer-generated hologram. *Opt Lett* 2011; **36**: 2943–2945.
- 41 Salter PS, Booth MJ. Dynamic optical methods for direct laser written waveguides. Proceedings of SPIE 8613, Advanced Fabrication Technologies for Micro/Nano Optics and Photonics VI, 86130A, 5 March 2013; San Francisco, CA, USA, SPIE: San Francisco, CA, USA, 2013.
- 42 Silvennoinen M, Kaakkunen J, Paivasaari K, Vahimaa P. Parallel femtosecond laser ablation with individually controlled intensity. *Opt Express* 2014; **22**: 2603–2608.
- 43 Thalhammer G, Bowman RW, Love GD, Padgett MJ, Ritsch-Marte M. Speeding up liquid crystal SLMs using overdrive with phase change reduction. *Opt Express* 2013; **21**: 1779–1797.
- 44 Joglekar AP, Liu HH, Meyhöfer E, Mourou G, Hunt AJ. Optics at critical intensity: applications to nanomorphing. *Proc Natl Acad Sci USA* 2004; **101**: 5856–5861.
- 45 Hayasaki Y, Nishitani M, Takahashi H, Yamamoto A, Takita H *et al*. Experimental investigation of the closest parallel pulses in holographic femtosecond laser processing. *Appl Phys A* 2012; **107**: 357–362.



This work is licensed under a Creative Commons Attribution-NonCommercial-ShareAlike 4.0 International License. The images or other third party material in this article are included in the article's Creative Commons license, unless indicated otherwise in the credit line; if the material is not included under the Creative Commons license, users will need to obtain permission from the license holder to reproduce the material. To view a copy of this license, visit <http://creativecommons.org/licenses/by-nc-sa/4.0/>

© The Author(s) 2018

Supplementary Information for this article can be found on the *Light: Science & Applications*' website (<http://www.nature.com/lsa>).